

Visible-Thermal Tiny Object Detection: A Benchmark Dataset and Baselines

Xinyi Ying, Chao Xiao, Ruoqing Li, Xu He, Boyang Li, Zhaoxu Li, Yingqian Wang, Mingyuan Hu, Qingyu Xu, Zaiping Lin, Miao Li, Shilin Zhou, Wei An, Weidong Sheng, Li Liu

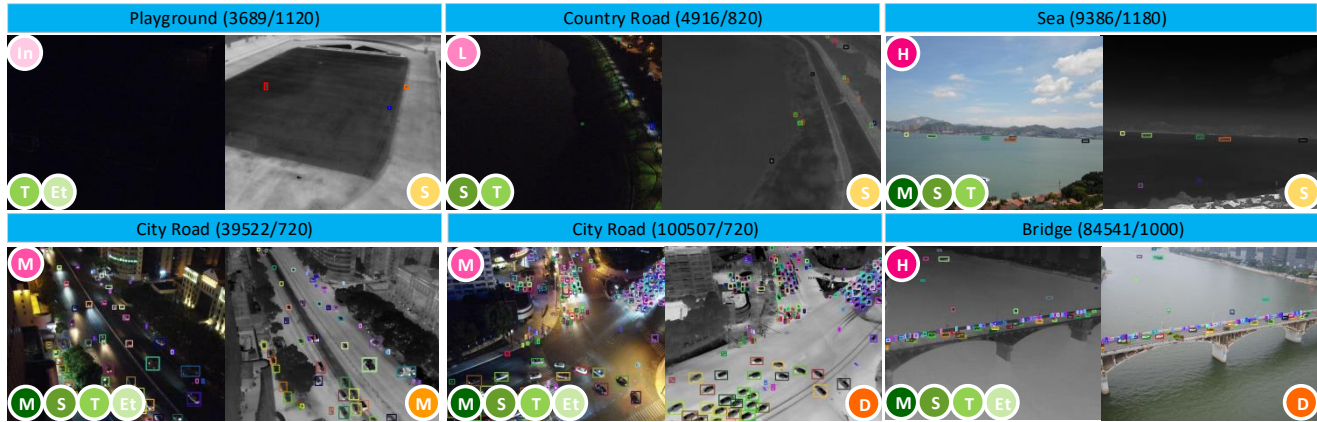


Fig. 1: Example frames of our RGBT-Tiny dataset. Scenes (annotation / frame number) are shown on the top. Sequence-level attributes are shown at the bottom. Pink, green and yellow circles represent levels of light vision (*i.e.*, H: high, M: medium, L: low, In: invisible), target size (*i.e.*, Et: extremely tiny, T: tiny, S: small, M: medium, L: large) and annotation density (*i.e.*, S: sparse, M: medium, D: dense).

Abstract—Small object detection (SOD) has been a longstanding yet challenging task for decades, with numerous datasets and algorithms being developed. However, they mainly focus on either visible or thermal modality, while visible-thermal (RGBT) bimodality is rarely explored. Although some RGBT datasets have been developed recently, the insufficient quantity, limited category, misaligned images and large target size cannot provide an impartial benchmark to evaluate multi-category visible-thermal small object detection (RGBT SOD) algorithms. In this paper, we build the first large-scale benchmark with high diversity for RGBT SOD (namely RGBT-Tiny), including 115 paired sequences, 93K frames and 1.2M manual annotations. RGBT-Tiny contains abundant targets (7 categories) and high-diversity scenes (8 types that cover different illumination and density variations). Note that, over 81% of targets are smaller than 16×16 , and we provide paired bounding box annotations with tracking ID to offer an extremely challenging benchmark with wide-range applications, such as RGBT fusion, detection and tracking. In addition, we propose a scale adaptive fitness (SAFit) measure that exhibits high robustness on both small and large targets. The proposed SAFit can provide reasonable performance evaluation and promote detection performance. Based on the proposed RGBT-Tiny dataset and SAFit measure, extensive evaluations have been conducted, including 23 recent state-of-the-art algorithms that cover four different types (*i.e.*, visible generic detection, visible SOD, thermal SOD and RGBT object detection). Project is available at <https://github.com/XinyiYing/RGBT-Tiny>.

Index Terms—Visible-Thermal, Tiny Object Detection, Benchmark Dataset.

1 INTRODUCTION

Small objects, featured by their extremely small size (*e.g.*, less than 32×32 pixels [1]), are always difficult to detect. Small Object Detection (SOD) has received significant attention in

recent years and becomes a challenging direction independent of generic object detection due to its valuable applications, including video surveillance [2, 3], autonomous driving [4, 5] and water rescue [6, 7]. Currently, the advancement of SOD faces the following challenges. First, the extremely small size with significantly fewer appearance cues raises serious limitations for feature representation learning, whereas the complex background clutter negatively affects the detection of small objects, and can cause many false alarms. Second, the lack of large-scale, high-quality datasets greatly hinders the advancement of SOD. Finally, the IOU-based evaluation metrics commonly used for generic object detection have

- This work was supported by the National Natural Science Foundation of China under Grant 62376283, and the Independent Innovation Science Fund Project of National University of Defense Technology (NUDT) under Grant 22-ZZCX-042. X. Ying (yingxinyi18@nudt.edu.cn), C. Xiao (xiaochao12@nudt.edu.cn), R. Li, X. He, B. Li, Z. Li, Y. Wang, M. Hu, Z. Li, Q. Xu, Z. Lin, M. Li, S. Zhou, W. An, W. Sheng (shengweidong1111@sohu.com), and L. Liu (liuli_nudt@nudt.edu.cn) are with the College of Electronic Science and Technology, NUDT, Changsha 410073, China. Xinyi Ying and Chao Xiao share the equal contribution. Li Liu and Weidong Sheng are the corresponding authors.

a low tolerance for bounding box (bbox) perturbation of small objects and cannot guarantee high localization accuracy. Therefore, in this paper, we aim to address the aforementioned challenges to advance the development of SOD by firstly building a large-scale dataset for SOD, then developing a novel evaluation metric for SOD named scale adaptive fitness (SAFit) measurement, and finally extensively evaluating various deep feature learning methods for SOD with the developed dataset and the proposed SAFit metric.

We build a new large-scale dataset for SOD that addresses the following core issues. Firstly, most existing studies focus on either visible [8, 9, 10, 11] or thermal [12, 13, 14] modality independently, and few research is conducted to explore the multimodal information fusion within visible-thermal (RGBT) bimodality [15, 16, 17]. Secondly, although various datasets [6, 18] have been proposed in visible [2, 3, 4, 5, 6, 7, 19, 20, 21, 22] and thermal [12, 13, 14, 23, 24, 25, 26, 27, 28, 29, 30] modalities, the limited quantity [3, 14], imbalanced distribution [7, 14], unitary pattern [21, 25] and low temporal consistency [7, 13] hinder the development of corresponding algorithms. Thirdly, existing RGBT datasets are either unpaired [31, 32], or designed for specific tasks (*i.e.*, single-object tracking with large size [33, 34, 35], pedestrian and vehicle detection [36, 37, 38]), which cannot provide an impartial benchmark for performance evaluation. The aforementioned issues urge us to build the first large-scale benchmark with high diversity for RGBT SOD (namely RGBT-Tiny), which can promote the development of both unimodal SOD in visible and thermal modalities and multimodal RGBT fusion, detection and tracking.

We propose a new measure SAFit to guarantee high robust evaluation on both large and small targets. Specifically, SAFit performs size-aware sigmoid weighted summation between large object-friendly IoU measure and small object-friendly NWD [39] measure, which can rapidly switch to an appropriate measure according to the corresponding bbox size. The switch point is flexibly controlled by a size-aware parameter C for custom requirements. In addition, a corresponding SAFit loss is developed and is demonstrated to benefit the detection performance.

Based on the proposed new dataset RGBT-Tiny and new metric SAFit, we conducted extensive performance evaluations on 23 recent state-of-the-art algorithms to provide a benchmark that spans over visible generic detection [40, 41, 42, 43, 44, 45, 46, 47, 48, 49, 50, 51, 52, 53], visible SOD [8, 9], thermal SOD [13, 24, 54], and RGBT object detection [55, 56]. Section 4.2 illustrates some discoveries of our benchmark, and we believe more discoveries and conclusions will emerge in the future.

The main contributions are summarized as follows: 1) We build the first large-scale benchmark with high diversity (*i.e.*, RGBT-Tiny) for RGBT SOD, including 115 paired sequences, 93K frames and 1.2M manual annotations. As compared with 26 existing benchmark datasets (including visible SOD, thermal SOD, RGBT detection and RGBT tracking datasets), RGBT-Tiny is finely aligned, and contains abundant small targets, high diversity scenes and high-quality annotations, as shown in Fig. 1. 2) We propose a scale adaptive fitness (SAFit) measure that exhibits high robustness to both large and small targets. The proposed SAFit can provide

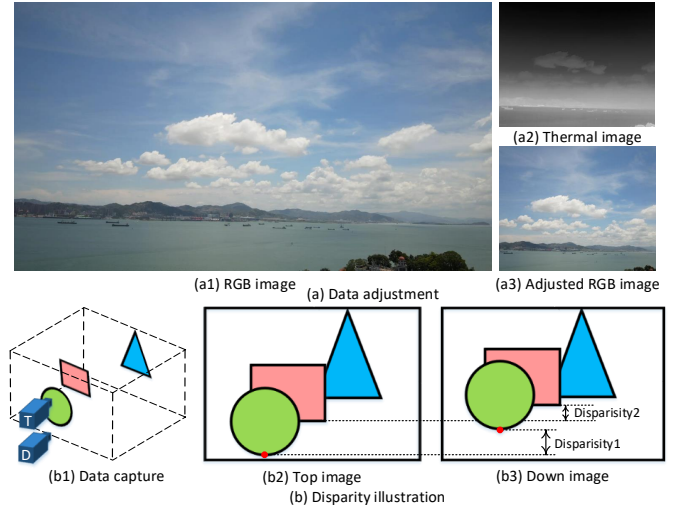


Fig. 2: (a1) Raw RGB image is aligned to (a2) thermal image to generate (a3) adjusted RGB image. (b) An illustration of disparity variations of dual lenses.

reasonable performance evaluation, and promote detection performance when equipped during training. 3) Based on the proposed RGBT-Tiny dataset and SAFit measure, we make comprehensive evaluations on 23 current state-of-the-art algorithms, including visible generic detection, visible SOD, thermal SOD and RGBT object detection methods, which lays solid foundations for further research.

2 RELATED WORK

RGBT Datasets. Early RGBT datasets [36, 58, 60, 61] cannot satisfy the “data hunger” of recent deep learning-based methods due to insufficient quantity and limited category. Then large-scale datasets [29, 31, 32, 33, 34, 35, 37, 38, 57, 59, 62, 63] with abundant targets & scenes and various applications have been proposed. However, these datasets are either unpaired [29, 31, 32], or designed for specific applications such as single-object tracking [29, 33, 34, 35, 57], pedestrian [37, 59] and vehicle detection [32, 62, 63], which can not provide an impartial benchmark to evaluate multi-category RGBT SOD algorithms.

RGBT Object Detection. To combine both advantages of visible and thermal modalities, RGBT datasets [37, 38, 59] emerge and promote the development of RGBT object detection methods [55, 56, 64, 65]. However, RGBT object detection always focuses on specific tasks (*e.g.*, pedestrian [64, 65] and vehicle [55, 66] detection), which lacks comprehensive benchmarks for the development of multi-category RGBT SOD algorithms. In addition, compared to generic SOD, RGBT SOD exhibits more challenges, including spatio-temporal misalignment, illuminance & density variance, and efficient multi-modal fusion.

Evaluation Metrics. Intersection over union (IoU), average precision (AP) and recall (AR) based on bounding boxes (bbox) are widely used evaluation metrics of Visible SOD [6, 18]. Based on IoU, numerous modified versions have been proposed, including generalized IoU (GIoU) [67], distance

TABLE 1: Statistical comparison among existing RGB SOD datasets (RGB-SOD), thermal SOD datasets (T-SOD), RGBT tracking datasets (RGBT-T), RGBT detection datasets (RGBT-D) and our RGBT-Tiny dataset. “Seq.”, “Frame”, “Anno.”, “T-Cat.” and “S-Cat.” represent the number of sequences, frames, annotations, target & scene categories, respectively. “FPS” is frame per second of released video sequences. “Split” represents the way of data split. “Align” represents whether RGBT images are aligned (Y) or not (N). “ID” represents providing tracking ID (Y) or not (N).

Benchmark	Seq.	Frame	Anno.	Resolution	FPS	T-Cat.	S-Cat.	Split	Align	ID	Year	
RGB-SOD	SODA-D [6]	-	24K	278K	3407×2470	-	9	-	train/val/test	-	-	2023
	SODA-A [6]	-	2.5K	800K	4761×2777	-	9	-	train/val/test	-	-	2023
	TJU-DHD Traffic [4]	-	60K	332K	1624×1200	-	5	-	train/val	-	-	2021
	SODA-10M [5]	-	10K	13K	1920×1080	-	6	-	train/val	-	-	2021
	VisDrone [2]	-	40	183K	3840×2160	-	10	-	train/val/test-c/test-d	-	-	2021
	DOTA v2 [7]	-	11k	1.8M	800 ² -4000 ²	-	18	-	train/val/test-c/test-d	-	-	2021
	WiderPerson [19]	-	13k	400K	Varied	-	1	-	train/val/test	-	-	2020
	EuroCity Persons [22]	-	47k	211K	1920×1024	-	3	-	train/val/test	-	-	2020
	WiderFace [21]	-	32K	394K	Varied	-	1	61	train/val/test	-	-	2016
MS-COCO [1]	-	328k	2.5M	Varied	-	91	-	train/val/test	-	-	2014	
T-SOD	IRSTD-1K [12]	-	1K	1.5K	512×512	-	1	6	train/val/test	-	-	2022
	NUDT-SIRST [13]	-	1.3K	1.9K	256×256	-	1	5	train/test	-	-	2022
	NUAA-SIRST [24]	-	427	480	Varied	-	1	3	train/val/test	-	-	2021
	Fu [30]	87	22K	89K	640×512	35	1	2	train/val	-	-	2022
	SIATD [26]	350	150K	247K	640×512	30	1	3	train/test	-	-	2021
Hui [27]	22	16K	17K	256×256	100	2	-	-	-	-	2020	
RGBT-T	VTUAV [35]	500	3.3M	326K	1920×1080	30	13	15	train/test	Y	N	2022
	Anti-UAV v1 [29]	318	586K	586K	640×512	20	1	-	train/val/test	N	N	2022
	LasHeR [57]	1224	6.7M	6.7M	630×480	-	32	20+	train/test	Y	N	2021
	VOT-RGBT [58]	60	40K	40K	630×460	20	13	-	-	Y	N	2020
RGBT234 [34]	234	234K	234K	630×460	30	22	-	-	Y	N	2019	
RGBT-D	LLVIP [37]	-	34K	-	1080×720	-	1	-	-	Y	-	2021
	VEDAI [32]	-	1.2K	3.7K	512 ² -1024 ²	-	9	-	train/test	N	-	2016
	CVC-14 [59]	4	17K	18K	640×512	10	1	-	train/test	Y	-	2016
	KAIST [38]	41	191K	103K	640×480	20	3	-	train/test	Y	-	2015
	FLIR [31]	7498	26K	520K	640×512	24	15	-	train/val	N	-	-
RGBT-Tiny	115	93K	1.2M	640×512	15	7	8	train/test	Y	Y	2024	

IoU (DIoU) [68] and complete-IoU (CIoU) [68]. However, these metrics focus on non-overlapping bboxes, but cannot well address the inherent problem of low tolerance for bbox perturbation. Therefore, novel evaluation metrics tailored for SOD are absolutely necessary.

3 RGBT-TINY BENCHMARK

3.1 Data Collection and Annotations

Data Capture. We employ a professional UAV DJI Mavic 2 as the data acquisition platform to ensure stable flight in extreme conditions. Vertically arranged RGBT dual lenses are equipped in UAV to collect RGBT video sequences from an altitude of 60-100 meters. The frame rate of visible and thermal cameras is 30, and we sample the video sequence to 15 frame per second (FPS) in the public videos for more obvious temporal motion. Thermal camera has a wavelength of 8-14 μm , and the image sizes between visible and thermal cameras are different (*i.e.*, 1080×1920 of RGB images and 512×640 of thermal images).

Data Adjustment. Camera calibration [69] is first applied to remove lens distortion in RGBT images. Then, we employ homography transformation [70] to align RGB images to thermal images since the positions of RGBT cameras are relatively fixed. To address the resolution difference between RGBT images, we crop the aligned RGB image patches that are consistent with thermal images to generate paired RGBT images with a resolution of 640×512. The adjusted RGBT images are shown in Fig. 2 (a). Note that, homography transformation can only perform frame alignment within a fixed depth of field (DoF). Therefore, the inherent disparity variations (shown in Fig. 2 (b)) of dual lenses [71] have not been well solved, and is a challenge that deserves investigation.

Groundtruth Annotations. We use DarkLabel [72] to annotate the groundtruth bbox with corresponding category and tracking ID. Note that, except for a few unrecognizable annotations in extreme conditions, RGBT annotations are paired within one-to-one correspondence. For quality assurance, we spent over 2000 hours conducting two-step verification. 1) Ten professional annotators make annotations respectively, and review one other annotator. 2) Each image is evaluated by another 2 assessors (5 assessors in total), and annotations are constantly revisited until without skeptic.

Training and Test Sets. To avoid data bias and over-fitting, training and test sets are split for 85 and 30 video sequences by the following criterion. 1) Each subset covers all types of scenes and objects. 2) Each subset covers all illumination and density variations. 3) Two subsets are not overlapped.

3.2 Benchmark Properties and Statistics

Rich Diversity. As shown in Fig. 3 (a), targets can be divided into 7 categories (*e.g.*, ship, car, cyclist, pedestrian, bus, drone and plane). It can be observed that despite generally consistent, the number of annotations in thermal images is higher (*e.g.*, ship and pedestrian) than those in visible images. This is because, as shown in Fig. 3 (b), our dataset covers different light visions (*i.e.*, high-light vision is captured in the daytime, and medium-light, low-light & invisible visions are captured at night), and thermal images can provide additional supplemental information under low-light and invisible visions. Note that, night-time sequences occupy 33.9% of all data, and over 70% of them are in low-light and invisible visions. Sequences are captured at 8 types of scenes (*i.e.*, sea, lake, bridge, city road, country road, playground, airport and sky) across four cities over a period of one year

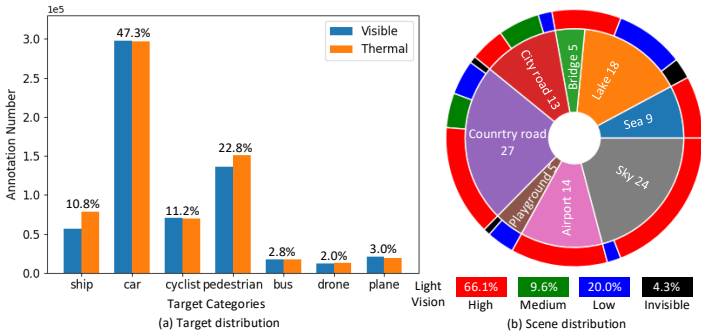


Fig. 3: (a) Annotation numbers w.r.t. target categories in visible and thermal modalities. Numbers represent the proportion of each category in annotations. (b) Inner circle shows sequence numbers w.r.t. scene categories, and outer circle shows the light vision distribution of scenes. Numbers in the pie chart represent the number of sequences of each scene type. Numbers in the legend represent the proportion of each light vision in annotations.

to obtain data in different seasons, weathers and locations. Comparisons among existing datasets are listed in table 1. In conclusion, we provide the first, large-scale, finely-aligned, RBGT SOD datasets with abundant targets & scenes and high-quality annotations, which facilitates the development of RBGT fusion, detection and tracking.

Large Density Variation. Fig. 4 (a) shows the average annotation number per frame (*i.e.*, density) of each sequence, and we divide density into three levels: sparse $\in[1,10)$, medium $\in[10,50)$, dense $\in[50,\infty)$. It can be observed that our dataset covers a large range of annotation density (from 1 to 161), and density varies greatly among different scenes. Specifically, the density of city road and bridge are much higher than that of sky and airport due to their unique targets and applications, which can provide valuable priors for object detection.

Small-Scale Targets. Following general scale ranks¹ of [1], we further divide the small scale into three levels: extremely tiny $\in[1^2,8^2)$, tiny $\in[8^2,16^2)$, small $\in[16^2,32^2)$. Fig. 4 (b) shows the annotation number with respect to (w.r.t.) the scale of each target category. It can be observed that tiny targets occupy the largest proportion (*i.e.*, 48%) and over 97% of targets are within small or smaller scales. In addition, due to different angles (*i.e.*, up, front and down) and distance of data acquisition, the absolute target size in image is different from the real target size. For example, larger planes are mostly divided into extremely tiny scale due to far-front handheld capture, and smaller buses are mostly divided into small scale due to close-down flight capture. In conclusion, targets cannot be simply classified by their absolute sizes. Comprehensive properties including appearance, density and trajectory should be considered for accurate detection.

Temporal Occlusion. For short-time occlusion (less than 5 frames), we employ temporal interpolation of bboxes [72] to maintain consistency. For long-time occlusion (more than 5 frames), occluded frames remain unsolved. Among all annotations, 3.4% are slightly occluded (5-10 frames), 3.4%

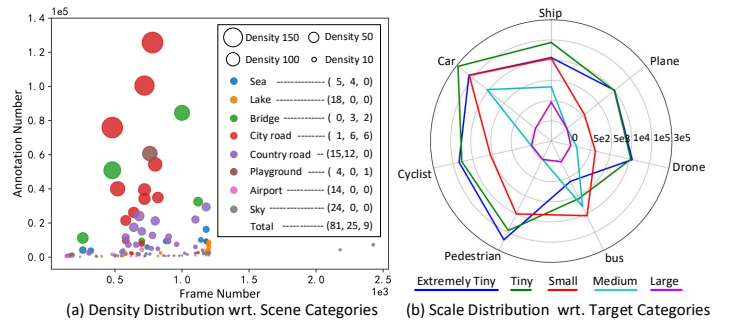


Fig. 4: (a) Average annotation number per frame (*i.e.*, density) of each sequence. Larger circle represents higher density, and different colors represent different scene types. (x,y,z) are the numbers of sequences w.r.t. density levels (*i.e.*, sparse, medium, dense). (b) Size distribution of each target category. Lines with different colors represent different scale levels. Radius represents the annotation number, and the area under each color line represents the total annotation number of each scale level.

are moderately occluded (10-20 frames) and 5.2% are heavily occluded (more than 20 frames).

3.3 Scale Adaptive Fitness Measure

Normalized Wasserstein distance (NWD) [39] has been demonstrated to be friendly to SOD due to scale invariance and smoothness to location deviation. The formulation can be defined as:

$$\text{NWD}(K) = \exp\left(-\frac{\sqrt{W_2^2(\mathcal{N}_p, \mathcal{N}_{gt})}}{K}\right), \quad (1)$$

$$W_2^2(\mathcal{N}_p, \mathcal{N}_{gt}) = \left\| \left(\mathcal{N}_p^T, \mathcal{N}_{gt}^T \right) \right\|_2^2, \quad (2)$$

where $W_2^2(\mathcal{N}_p, \mathcal{N}_{gt})$ is the Wasserstein distance between the Gaussian distributions of predicted bbox $\mathcal{N}_p = [cx_p, cy_p, w_p/2, h_p/2]$ and groundtruth (GT) bbox $\mathcal{N}_{gt} = [cx_{gt}, cy_{gt}, w_{gt}/2, h_{gt}/2]$ with center point locations of (cx, cy) , width w and height h . K is a hyperparameter closely related to the dataset [39]. However, the scale-invariant absolute distance measure cannot provide reasonable evaluation for targets with large sizes.

Intersection over union (IoU) [18] is a common and reasonable metric for performance evaluation on large generic objects. The formulation can be defined as:

$$\text{IoU} = \frac{S_p \cap S_{gt}}{S_p \cup S_{gt}}, \quad (3)$$

where S_p and S_{gt} represent the predicted and groundtruth bboxes. Despite scale invariance, symmetry and other advantages, IoU shows low tolerance for bbox perturbation of small objects, as shown in Fig. 5 (b). A minor location deviation (*e.g.*, 2 pixels deviation for a tiny object of size 8×8) can lead to a notable IoU drop (*e.g.*, from 1 to 0.39). In conclusion, IoU-based metrics are not suitable for evaluating the performance of SOD.

To combine both advantages of IoU and NWD while avoiding drawbacks, we develop a scale adaptive fitness

1. small $\in[1^2,32^2)$, medium $\in[32^2,96^2)$ and large $\in[96^2,\infty)$

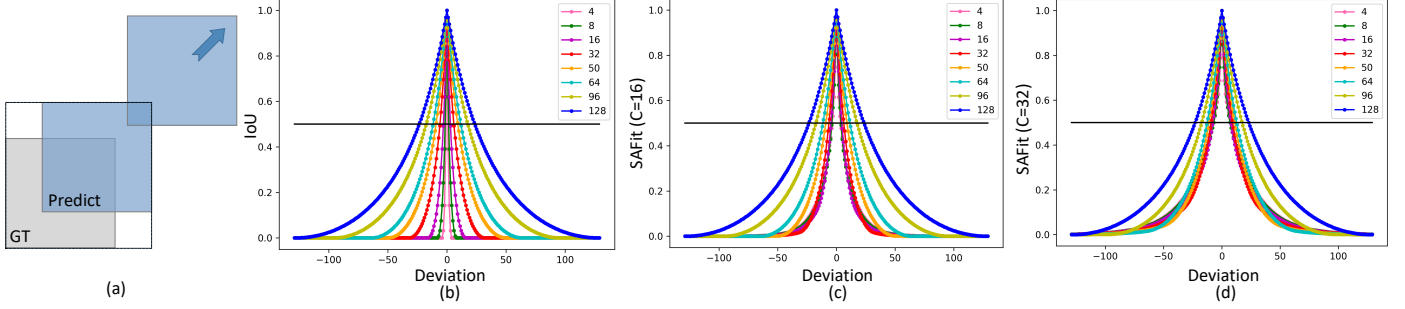


Fig. 5: (a) An illustration of the pixel deviation between the center points of GT bbox and predicted bbox. (b) IoU-Deviation curves w.r.t different sizes of bboxes. (c)-(d) SAFit-Deviation curves under different C values. The abscissa value represents the number of pixels deviation. The ordinate value represents the corresponding metric value. Note that, since the locations of bboxes can only change discretely, curves are presented as scatter diagrams.

(SAFit) measure that exhibits high robustness to both large and small targets. Specifically, we combine IoU and NWD via size-aware Sigmoid weighted summation:

$$\text{SAFit} = \frac{1}{1 + e^{-(\sqrt{A}/C-1)}} \times \text{IoU} + \left(1 - \frac{1}{1 + e^{-(\sqrt{A}/C-1)}}\right) \times \text{NWD}(C), \quad (4)$$

where Sigmoid function indicates a soft switch, which can rapidly switch to an appropriate measure by corresponding bbox size. A is the area of GT bbox and C is a constant that balances NWD and IoU measures in a size-aware manner. That is, when $A = C^2$, NWD and IoU share equal contributions. A lower value of A (*i.e.*, smaller size of GT bbox) leads to NWD domination, while a higher value results in an increased proportion of IoU. In conclusion, SAFit is practical for real applications that contain targets with varied categories and sizes.

Quantitative comparisons among IoU and SAFit under different C values (*i.e.*, 16, 32) are shown in Fig. 5. It can be observed that when the size of GT bbox is larger than C , SAFit is consistent with IoU. As GT bbox size decreases, SAFit rapidly turns to a scale-invariant absolute distance measure of NWD, which is highly robust to bbox perturbation. Note that, through adjusting the value of C , SAFit can provide flexible applications for different custom requirements. For our dataset, we set $C = 32$ because small target is defined to be smaller than 32×32 . In addition, we develop SAFit loss (*i.e.*, $L_{\text{SAFit}} = 1 - \text{SAFit}$) for network training, which can provide stable and accurate optimization guidance on targets with varied sizes. Note that, each component (*i.e.*, IoU and NWD) of SAFit loss can be flexibly replaced by new measures.

4 EXPERIMENTS

4.1 Scale Adaptive Fitness Measure

SAFit Measure for Evaluation. We employ IoU, NWD and SAFit measures for performance evaluation on three recent state-of-the-art generic detection methods (*i.e.*, Cascade RCNN [45], FCOS [49], and Deformable DETR [52]). More results on other methods are listed in supplemental materials. AP results in visible and thermal modalities across different target scales are shown in Fig. 6. It can be observed that when the size of

GT bbox is smaller than 32×32 , AP values of IoU are much lower than those of NWD while an opposite result is obtained within medium and large targets. This phenomenon intuitively shows the unreasonable evaluation of IoU on small objects and NWD on large objects. Note that, AP values of SAFit are closer to those of NWD when GT bbox size is small, and rapidly switch to those of IoU as size increases, which is consistent with the quantitative analyses in Fig. 5. In conclusion, SAFit shows comprehensively reasonable evaluations on both large and small targets, which exhibits high practical value. To this end, all experimental results below are evaluated under SAFit measure if not specified.

SAFit Loss for Training. We equip different losses (*i.e.*, IoU [18], DIoU [68], CIoU [68], GIoU [67], NWD [39] and SAFit losses) with different detectors (*i.e.*, ATSS [50], SparseRCNN [53], and train the network under the same settings in visible modality. Note that, we employ 2 variants of SAFit loss (*i.e.*, SAFit-s and SAFit-g) to investigate the performance of direct transition (*i.e.*, loss function is set to NWD when GT box size is smaller than C , while set to IoU vice versa) and stronger component (*i.e.*, Sigmoid weighted summation of GIoU and NWD). SAFit-based results are shown in table 2. Please refer to supplemental materials for corresponding IoU-based results. It can be observed that SAFit loss shows high robustness to different detectors under both IoU and SAFit metrics. In addition, compared with SAFit-s loss, SAFit loss achieves higher AP values, which demonstrates that size-aware weighted summation is superior to direct transition. Moreover, SAFit-g performs superior to SAFit, which demonstrates that stronger components further promote the detection performance. Furthermore, compared with its components, SAFit-g and SAFit achieves higher AP_{et}^s , AP_t^s values than NWD, and higher AP_m^s values than GIoU and IoU respectively, which demonstrates that our size-aware weighted summation can not only combine both advantages of its components but also produce a breakthrough by offering a more stable and smooth training for targets with varied sizes.

4.2 Baseline Results

We conduct comprehensive evaluations on 23 recent state-of-the-art detection methods, including 14 visible generic object

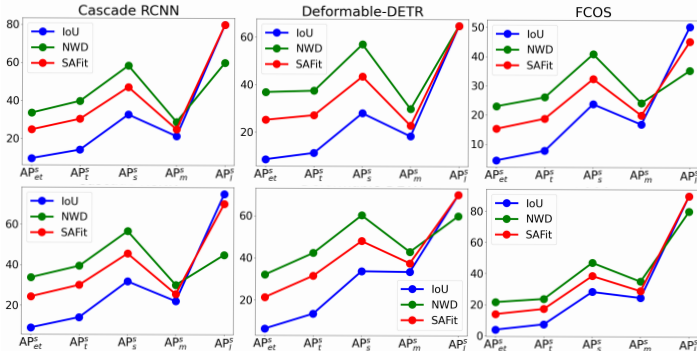


Fig. 6: Comparisons among different measures for performance evaluation in visible and thermal modalities. $AP^{s_{et}}$, AP^t , AP^s , AP^m , AP^l represent AP values of extremely tiny, tiny, small, medium, large targets.

detection methods² (e.g., SSD [40], YOLO [41], TOOD [42], Faster RCNN [43], SABL [44], Cascade RCNN [45], Dynamic RCNN [46], RetinaNet [47], CenterNet [48], FCOS [49], ATSS [50], VarifocalNet [51], Deformable DETR [52] and Sparse RCNN [53]), 3 visible SOD methods³ (e.g., RFLA [8], QueryDet [9], C3Det [10]), 3 thermal SOD methods⁴ (e.g., DNAnet [13], ALCNet [54], ACM [24]) and 3 RGBT detection methods³ (e.g., UA-CMDet [55], ProbEn-early [56], ProbEn-middle [56]). In addition, we also evaluate different MOT algorithms on RGBT-Tiny, please refer to the supplemental materials.

Note that, thermal SOD methods can only perform foreground and background segmentation. For performance evaluation on multi-category bboxes, we first enlarge the output channels of CNN-based thermal SOD models to perform multi-category segmentation. Then we employ uniform and Gaussian distribution to generate hard (i.e., all pixels in bboxes are assigned to be positive pixels) and soft (i.e., pixels in bboxes are assigned to probability values under Gaussian distribution [39]) mask annotations of each category for training. For test, we transfer the multiclass segmentation output masks to bboxes via the minimum enclosing rectangle of each connected region.

SAFit-based results are shown in tables 3, and IoU-based results are listed in supplemental materials. From the experimental results, several phenomena and corresponding conclusions can be obtained: 1) RFLA achieves the highest AP scores in visible and thermal modalities, which demonstrates that small object-specific designs are significant for performance improvements on RGBT-Tiny benchmark. C3Det performs inferior because C3Det focuses on interactive annotation to alleviate annotation burden rather than small object-specific designs. 2) The highest AP scores of RGBT-Tiny benchmark are much lower than other public benchmarks [1, 7, 13, 38], which demonstrates that RGBT-Tiny is an extremely challenging benchmark due to extremely small targets, low-light vision, dense annotations, occluded targets and RBGT

2. All models are implemented by mmdetection code library [73] under their default parameters (ResNet50 [74] and FPN [75] are preferred as the backbone and neck) and training settings. We reduce the initial anchor size of two-stage methods to adapt to small targets.

3. All models are implemented by their officially public codes.

4. All models are implemented by BasicRSTD code library [76] under their default settings.

TABLE 2: SAFit-based results of different losses equipped with different detectors. SAFit-s, SAFit_g are used to investigate the effect of direct transition and stronger components.

Loss	ATSS						Sparse RCNN							
	AP	AP ₅₀	AP _{et} ^s	AP _t ^s	AP _s ^s	AP _m ^s	AP	AP ₅₀	AP _{et} ^s	AP _t ^s	AP _s ^s	AP _m ^s	AP _l ^s	
GIoU [67]	24.2	38.1	19.6	23.6	43.8	27.5	65.0	19.2	29.8	18.8	19.5	33.4	14.9	40.1
DIoU [68]	23.6	37.5	19.2	23.1	43.6	28.2	80.0	19.1	29.7	19.7	18.5	33.9	14.7	60.1
CIoU [68]	24.2	39.1	19.6	24.2	42.6	29.0	65.0	20.0	30.6	19.5	19.0	33.9	14.8	80.1
IoU [1]	23.3	37.3	19.3	23.7	42.3	26.5	75.0	8.1	14.7	11.3	7.1	11.8	0.2	0.0
NWD [39]	24.1	38.6	19.6	23.6	44.2	27.0	60.0	19.7	30.2	19.7	18.4	35.8	15.2	50.0
SAFit-s	24.3	39.0	19.7	24.3	42.1	27.5	60.0	19.8	31.2	18.4	19.4	35.5	14.5	50.1
SAFit	24.5	39.2	19.7	25.1	43.5	28.0	60.1	21.4	32.2	20.4	20.5	36.3	14.5	15.0
SAFit _g	24.7	39.3	20.6	23.6	44.4	27.5	70.0	22.0	34.0	22.2	19.5	34.9	16.3	15.0

disparities. 3) Powerful end-to-end methods [52, 53] perform inferior to anchor-based two-stage methods [43, 44, 45, 46], which demonstrates that dynamic learnable proposals are inferior to densely arranged anchors on RGBT-Tiny benchmark due to less appearance of small objects. 4) Several paradigms can achieve superior performance, including region proposal refinement [44, 45, 46], multi-scale information fusion [40, 42, 52] and contextual information utilization [45, 52], which provides suggestions for further algorithm designs. 5) Soft masks, generated by bboxes under Gaussian distribution, can offer stable training for reasonable evaluation results, and thus breakthrough the evaluation gap between visible and thermal SOD methods. 6) Performance in visible modality is generally higher than that in thermal modality due to rich information and corresponding discriminative features of visible images. However, as shown in Figs. 7 (a) and (b), when encountering low-vision conditions, AP values in thermal modality are higher than those in visible modality due to insensitivity to illumination and weather. In addition, ATSS and VarifocalNet perform the opposite due to powerful label assignment strategy, which compensates the information difference between visible and thermal modalities. Since thermal modality can provide complementary information for performance improvements in low-vision conditions due to insensitivity to illumination and weather, higher values are obtained in thermal modality. 7) RGBT detection methods make full use of RGBT complementary information for performance improvements in both modalities, as shown in table 3 and Fig. 7 (c). Note that, RGBT fusion in ProbEn-early and UA-CMDet introduce performance degradation in both modalities. This is because, easy image-level fusion cannot well address the large illumination & disparity variations in our dataset, and IoU-based uncertainty-aware module cannot provide accurate fusion clues.

5 CONCLUSION

In this paper, we build the first large-scale benchmark (i.e., RGBT-Tiny) for RGBT-SOD. RGBT-Tiny is an extremely challenging benchmark that contains abundant targets and diverse scenes that cover large density and illumination variations. RGBT-Tiny provides paired instance bbox annotations with tracking ID to span over large application scopes, including RGBT fusion, detection and tracking. In addition, we propose a scale adaptive fitness measure (SAFit) that exhibits high robustness to both large and small targets, which can provide reasonable performance evaluation and optimal training process. Based on the proposed RGBT-Tiny dataset

TABLE 3: SAFit-based results of existing visible generic detection (V-D), visible SOD (V-SOD), thermal SOD (T-SOD), visible-thermal detection methods (VT-D) methods on RGBT-Tiny dataset. “#Param.” represents the number of parameters. AP_{et}^s , AP_{t}^s , AP_s^s , AP_m^s , AP_l^s represent AP values of extremely tiny, tiny, small, medium, large targets. “(-)” represents network trained under replicated visible or thermal inputs to investigate the influence of RGBT fusion. Note that, the results of T-SOD are trained with hard (left) and soft (right) masks generated by bboxes under uniform and Gaussian distributions.

	Methods	#Param.	Visible									Thermal								
			AP	AP ₅₀	AP ₇₅	AP _{et} ^s	AP _t ^s	AP _s ^s	AP _m ^s	AP _l ^s	AR	AP	AP ₅₀	AP ₇₅	AP _{et} ^s	AP _t ^s	AP _s ^s	AP _m ^s	AP _l ^s	AR
V-D	SSD [40]	25.2M	28.0	43.1	31.9	24.2	26.6	41.9	22.7	45.0	36.8	27.0	42.0	31.8	20.2	29.5	45.7	34.8	30.0	35.9
	YOLO [41]	61.5M	24.3	37.7	28.4	21.4	25.1	35.8	20.5	60.1	30.5	24.1	36.7	28.4	18.5	29.5	40.2	26.3	50.0	30.9
	TOOD [42]	31.8M	27.9	43.5	31.7	23.1	27.9	44.6	30.6	60.0	38.6	27.9	42.3	32.0	22.1	27.9	47.9	27.7	70.0	38.9
	ATSS [50]	31.9M	24.2	38.1	26.8	19.6	23.6	43.8	27.5	65.0	38.0	27.5	42.1	32.3	19.9	29.7	46.5	44.1	<u>80.0</u>	40.0
	RetinaNet [47]	36.2M	21.8	37.4	22.9	20.9	19.4	34.9	25.3	75.0	34.5	19.3	32.4	21.7	15.4	21.4	33.8	35.7	<u>80.0</u>	35.1
	Faster RCNN [43]	41.2M	28.8	43.1	33.5	24.3	30.1	44.2	22.0	65.0	37.2	29.5	43.0	<u>36.2</u>	21.9	35.2	45.0	41.4	<u>80.0</u>	36.4
	Cascade RCNN [45]	68.9M	30.1	44.2	35.8	24.8	30.4	47.1	25.0	80.0	37.4	30.0	44.2	34.9	24.7	29.8	46.6	25.8	90.0	37.4
	Dynamic RCNN [46]	41.2M	29.4	44.0	34.2	24.4	31.2	45.9	23.8	55.0	37.0	28.4	40.9	34.4	21.7	33.8	47.1	40.8	60.0	35.8
	SABL [44]	41.9M	29.6	43.3	35.3	24.0	<u>31.0</u>	46.6	25.5	77.6	37.1	29.3	42.2	35.7	21.8	34.8	47.2	42.6	90.0	36.6
	CenterNet [48]	14.4M	17.8	31.7	18.2	16.7	18.4	29.4	16.4	25.0	28.9	15.5	27.3	16.2	12.2	17.7	25.7	28.5	30.0	28.2
	FCOS [49]	31.9M	17.5	28.6	19.2	15.3	18.8	32.4	20.0	45.2	30.1	16.9	27.7	19.2	14.0	17.4	38.6	29.0	90.0	31.2
	VarifocalNet [51]	32.5M	26.9	41.6	30.1	22.1	27.8	45.0	27.9	80.0	<u>39.1</u>	<u>30.4</u>	45.8	36.5	20.2	34.7	51.4	46.8	90.0	<u>40.6</u>
	Deformable DETR [52]	39.8M	28.2	<u>45.4</u>	32.0	25.2	27.2	43.5	22.9	65.0	38.5	28.0	<u>44.2</u>	32.7	21.4	31.6	48.1	37.6	70.0	38.8
Sparse RCNN [53]	44.2M	19.2	29.8	21.9	18.8	19.5	33.4	14.9	40.1	33.7	20.6	31.5	24.0	18.0	22.4	31.6	31.0	40.0	36.1	
V-SOD	QueryDet [9]	39.4M	23.6	36.0	28.1	19.2	25.1	37.0	20.3	30.0	37.6	25.1	39.4	30.0	19.3	31.0	40.1	21.3	40.0	39.9
	RFLA [8]	36.3M	32.1	47.1	36.3	26.8	30.4	45.3	<u>29.4</u>	50.0	43.0	33.8	50.2	40.1	27.5	37.6	<u>49.8</u>	38.8	60.0	45.4
	C3Det [10]	55.3M	9.4	13.8	11.2	0.5	8.1	42.1	25.6	81.7	10.9	11.4	16.8	13.3	0.3	8.0	48.7	45.2	<u>80.0</u>	13.3
T-SOD	ACM [24]	0.4M	1.2	2.4	1.0	8.8	5.7	5.0	0.0	0.0	4.9	18.2	32.0	20.5	21.7	25.0	22.1	11.4	40.0	24.3
	ALCNet [54]	0.4M	2.0	5.7	0.5	19.6	9.3	2.0	0.0	0.0	8.6	12.2	22.0	11.9	13.9	15.3	17.8	7.2	19.3	22.0
	DNAAnet [13]	<u>4.7M</u>	2.6	4.8	2.5	1.0	4.4	6.2	14.5	0.0	8.3	13.6	22.0	15.1	14.9	13.8	31.3	14.3	0.0	27.7
VT-D	UA-CMDet (-) [55]	139.2M	18.4	30.2	20.4	11.7	22.5	41.8	21.0	52.1	24.3	24.4	37.9	29.7	14.1	20.9	47.2	42.5	20.3	31.3
	UA-CMDet [55]	139.2M	16.1	30.6	15.6	12.1	18.5	32.7	16.9	14.2	26.2	20.0	35.0	21.4	10.8	24.1	35.0	38.5	9.7	28.5
	ProbEn-early [56]	60.3M	18.4	28.3	22.4	14.5	22.0	32.1	19.5	80.0	23.5	17.0	26.8	19.4	12.3	20.2	32.3	22.2	76.7	22.2
	ProbEn-middle (-) [56]	120.6M	24.7	35.0	29.9	20.7	24.8	38.1	26.9	<u>85.0</u>	29.9	26.0	36.1	32.3	19.2	31.4	40.9	35.8	<u>80.0</u>	31.5
	ProbEn-middle [56]	120.6M	27.4	39.7	33.4	23.4	29.6	37.2	30.8	92.5	33.1	29.3	41.0	35.9	21.8	<u>35.3</u>	44.1	37.5	70.0	34.0

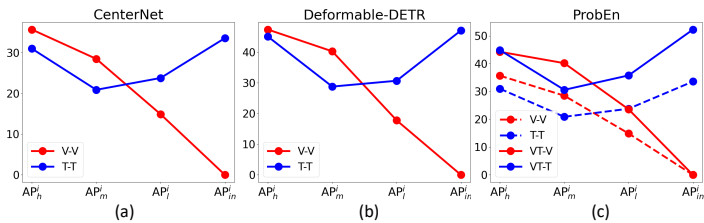


Fig. 7: Comparisons among different illumination conditions. “V-V”, “T-T” represent AP values of network trained and test by visible and thermal modalities, respectively. “VT-V”, “VT-T” represent AP values of network trained by visible-thermal images, and test in visible and thermal modalities, respectively. AP_h^i , AP_m^i , AP_l^i , AP_{in}^i represent AP values under high-light, medium-light, low-light, invisible illumination conditions.

and SAFit measure, we make comprehensive evaluations on 23 recent state-of-the-art detection algorithms. Note that, this work focuses on constructing a comprehensive benchmark with optimal evaluation metrics, and new baselines will be discussed in the future.

REFERENCES

- [1] T.-Y. Lin, M. Maire, S. Belongie, J. Hays, P. Perona, D. Ramanan, P. Dollár, and C. L. Zitnick, “Microsoft coco: Common objects in context,” in *ECCV*, 2014.
- [2] P. Zhu, L. Wen, D. Du, X. Bian, H. Fan, Q. Hu, and H. Ling, “Detection and tracking meet drones challenge,” *TPAMI*, 2021.
- [3] X. Yu, Y. Gong, N. Jiang, Q. Ye, and Z. Han, “Scale match for tiny person detection,” in *WACV*, 2020.
- [4] Y. Pang, J. Cao, Y. Li, J. Xie, H. Sun, and J. Gong, “Tju-dhd: A diverse high-resolution dataset for object detection,” *TIP*, 2020.
- [5] J. Han, X. Liang, H. Xu, K. Chen, L. Hong, J. Mao, C. Ye, W. Zhang, Z. Li, X. Liang *et al.*, “Soda10m: A large-scale 2d self-/semi-supervised object detection dataset for autonomous driving,” *Arxiv*, 2021.
- [6] G. Cheng, X. Yuan, X. Yao, K. Yan, Q. Zeng, and J. Han, “Towards large-scale small object detection: Survey and benchmarks,” *TPAMI*, 2023.
- [7] J. Ding, N. Xue, G.-S. Xia, X. Bai, W. Yang, M. Y. Yang, S. Belongie, J. Luo, M. Datcu, M. Pelillo *et al.*, “Object detection in aerial images: A large-scale benchmark and challenges,” *TPAMI*, 2021.
- [8] C. Xu, J. Wang, W. Yang, H. Yu, L. Yu, and G.-S. Xia, “Rfla: Gaussian receptive based label assignment for tiny object detection,” in *ECCV*, 2022.
- [9] C. Yang, Z. Huang, and N. Wang, “Querydet: Cascaded sparse query for accelerating high-resolution small object detection,” in *CVPR*, 2022.
- [10] C. Lee, S. Park, H. Song, J. Ryu, S. Kim, H. Kim, S. Pereira, and D. Yoo, “Interactive multi-class tiny-object detection,” in *CVPR*, 2022.
- [11] F. C. Akyon, S. O. Altinuc, and A. Temizel, “Slicing aided hyper inference and fine-tuning for small object detection,” *ICIP*, 2022.
- [12] M. Zhang, R. Zhang, Y. Yang, H. Bai, J. Zhang, and J. Guo, “Isnet: Shape matters for infrared small target detection,” in *CVPR*, 2022.
- [13] B. Li, C. Xiao, L. Wang, Y. Wang, Z. Lin, M. Li, W. An, and Y. Guo, “Dense nested attention network for infrared small target detection,” *TIP*, 2022.
- [14] H. Wang, L. Zhou, and L. Wang, “Miss detection vs. false alarm: Adversarial learning for small object segmentation in infrared images,” in *ICCV*, 2019.
- [15] S. Hwang, J. Park, N. Kim, Y. Choi, and I. So Kweon, “Multispectral pedestrian detection: Benchmark dataset and baseline,” in *CVPR*, 2015.
- [16] K. Zhou, L. Chen, and X. Cao, “Improving multispectral pedestrian detection by addressing modality imbalance problems,” in *ECCV*, 2020.
- [17] Y. Sun, B. Cao, P. Zhu, and Q. Hu, “Drone-based rgb-infrared cross-modality vehicle detection via uncertainty-aware learning,” *TCSVT*, 2022.
- [18] G. Chen, H. Wang, K. Chen, Z. Li, Z. Song, Y. Liu, W. Chen, and A. Knoll, “A survey of the four pillars for small object detection: Multiscale representation, contextual information, super-resolution, and region proposal,” *TSMC*, 2022.
- [19] S. Zhang, Y. Xie, J. Wan, H. Xia, S. Z. Li, and G. Guo, “Widerperson: A diverse dataset for dense pedestrian detection in the wild,” *TMM*,

- 2019.
- [20] C. Chen, M.-Y. Liu, O. Tuzel, and J. Xiao, "R-cnn for small object detection," in *ACCV*, 2017.
- [21] S. Yang, P. Luo, C.-C. Loy, and X. Tang, "Wider face: A face detection benchmark," in *CVPR*, 2016.
- [22] M. Braun, S. Krebs, F. Flohr, and D. M. Gavrila, "Eurocity persons: A novel benchmark for person detection in traffic scenes," *TPAMI*, 2019.
- [23] C. Gao, D. Meng, Y. Yang, Y. Wang, X. Zhou, and A. G. Hauptmann, "Infrared patch-image model for small target detection in a single image," *TIP*, 2013.
- [24] Y. Dai, Y. Wu, F. Zhou, and K. Barnard, "Asymmetric contextual modulation for infrared small target detection," in *WACV*, 2021.
- [25] T. Wu, B. Li, Y. Luo, Y. Wang, C. Xiao, T. Liu, J. Yang, W. An, and Y. Guo, "Mtu-net: Multi-level transunet for space-based infrared tiny ship detection," *ArXiv*, 2022.
- [26] X. Sun, L. Guo, W. Zhang, Z. Wang, Y. Hou, Z. Li, and X. Teng, "A dataset for small infrared moving target detection under clutter background," *CSD*, 2021.
- [27] B. Hui, Z. Song, H. Fan, P. Zhong, W. Hu, X. Zhang, J. Ling, H. Su, W. Jin, Y. Zhang, and Y. Bai, "A dataset for infrared detection and tracking of dim-small aircraft targets under ground / air background," *CSD*, 2020.
- [28] M. Zhao, L. Cheng, X. Yang, P. Feng, L. Liu, and N. Wu, "Tbc-net: A real-time detector for infrared small target detection using semantic constraint," *ArXiv*, 2019.
- [29] N. Jiang, K. Wang, X. Peng, X. Yu, Q. Wang, J. Xing, G. Li, Q. Ye, J. Jiao, Z. Han *et al.*, "Anti-uav: a large-scale benchmark for vision-based uav tracking," *TMM*, 2021.
- [30] R. Fu, H. Fan, Y. Zhu, B. Hui, Z. Zhang, P. Zhong, D. Li, S. Zhang, G. Chen, and L. Wang, "A dataset for infrared time-sensitive target detection and tracking for air-ground application," *CSD*, 2022.
- [31] FLIR, "Free teledyne flir thermal dataset for algorithm training," <https://www.flir.com/oem/adas/adas-dataset-form/>, 2018.
- [32] S. Razakarivony and F. Jurie, "Vehicle detection in aerial imagery: A small target detection benchmark," *JVCI*, 2016.
- [33] C. Li, N. Zhao, Y. Lu, C. Zhu, and J. Tang, "Weighted sparse representation regularized graph learning for rgb-t object tracking," in *ACM MM*, 2017.
- [34] C. Li, X. Liang, Y. Lu, N. Zhao, and J. Tang, "Rgb-t object tracking: Benchmark and baseline," *PR*, 2019.
- [35] P. Zhang, J. Zhao, D. Wang, H. Lu, and X. Ruan, "Visible-thermal uav tracking: A large-scale benchmark and new baseline," in *CVPR*, 2022.
- [36] R. I. Hammoud, J. W. David, and G. Fan, "Otcvbs benchmark dataset collection," <http://vcipl-okstate.org/pbvs/bench/>, 2004.
- [37] X. Jia, C. Zhu, M. Li, W. Tang, and W. Zhou, "Llvip: A visible-infrared paired dataset for low-light vision," in *ICCV*, 2021.
- [38] S. Hwang, J. Park, N. Kim, Y. Choi, and I. So Kweon, "Multispectral pedestrian detection: Benchmark dataset and baseline," in *CVPR*, 2015.
- [39] J. Wang, C. Xu, W. Yang, and L. Yu, "A normalized gaussian wasserstein distance for tiny object detection," *ArXiv*, 2021.
- [40] W. Liu, D. Anguelov, D. Erhan, C. Szegedy, S. Reed, C.-Y. Fu, and A. C. Berg, "Ssd: Single shot multibox detector," in *ECCV*, 2016.
- [41] J. Redmon, S. Divvala, R. Girshick, and A. Farhadi, "You only look once: Unified, real-time object detection," in *CVPR*, 2016.
- [42] C. Feng, Y. Zhong, Y. Gao, M. R. Scott, and W. Huang, "Tood: Task-aligned one-stage object detection," in *ICCV*, 2021.
- [43] S. Ren, K. He, R. Girshick, and J. Sun, "Faster r-cnn: Towards real-time object detection with region proposal networks," *TPAMI*, 2017.
- [44] J. Wang, W. Zhang, Y. Cao, K. Chen, J. Pang, T. Gong, J. Shi, C. C. Loy, and D. Lin, "Side-aware boundary localization for more precise object detection," in *ECCV*, 2020.
- [45] Z. Cai and N. Vasconcelos, "Cascade r-cnn: Delving into high quality object detection," in *CVPR*, 2018.
- [46] H. Zhang, H. Chang, B. Ma, N. Wang, and X. Chen, "Dynamic R-CNN: Towards high quality object detection via dynamic training," *ArXiv*, 2020.
- [47] T.-Y. Lin, P. Goyal, R. Girshick, K. He, and P. Dollár, "Focal loss for dense object detection," in *ICCV*, 2017.
- [48] X. Zhou, D. Wang, and P. Krähenbühl, "Objects as points," *ArXiv*, 2019.
- [49] Z. Tian, C. Shen, H. Chen, and T. He, "Fcos: Fully convolutional one-stage object detection," in *ICCV*, 2019.
- [50] S. Zhang, C. Chi, Y. Yao, Z. Lei, and S. Z. Li, "Bridging the gap between anchor-based and anchor-free detection via adaptive training sample selection," in *CVPR*, 2020.
- [51] H. Zhang, Y. Wang, F. Dayoub, and N. Sünderhauf, "Varifocalnet: An iou-aware dense object detector," *CVPR*, 2021.
- [52] X. Zhu, W. Su, L. Lu, B. Li, X. Wang, and J. Dai, "Deformable detr: Deformable transformers for end-to-end object detection," in *ICLR*, 2020.
- [53] P. Sun, R. Zhang, Y. Jiang, T. Kong, C. Xu, W. Zhan, M. Tomizuka, L. Li, Z. Yuan, C. Wang *et al.*, "Sparse r-cnn: End-to-end object detection with learnable proposals," in *CVPR*, 2021.
- [54] Y. Dai, Y. Wu, F. Zhou, and K. Barnard, "Attentional local contrast networks for infrared small target detection," *TGRS*, 2021.
- [55] Y. Sun, B. Cao, P. Zhu, and Q. Hu, "Drone-based rgb-infrared cross-modality vehicle detection via uncertainty-aware learning," *TCSVT*, 2022.
- [56] Y.-T. Chen, J. Shi, C. Mertz, S. Kong, and D. Ramanan, "Multimodal object detection via probabilistic ensembling," in *ECCV*, 2022.
- [57] C. Li, W. Xue, Y. Jia, Z. Qu, B. Luo, J. Tang, and D. Sun, "Lasher: A large-scale high-diversity benchmark for rgbt tracking," *TIP*, 2021.
- [58] M. Kristan, J. Matas, A. Leonardis, M. Felsberg, R. Pflugfelder, J.-K. Kamarainen, L. ˇCehovin Zajc, O. Drbohlav, A. Lukezic, A. Berg *et al.*, "The seventh visual object tracking vot2019 challenge results," in *ICCVW*, 2019.
- [59] A. González, Z. Fang, Y. Socarras, J. Serrat, D. Vázquez, J. Xu, and A. M. López, "Pedestrian detection at day/night time with visible and fir cameras: A comparison," *Sensors*, 2016.
- [60] A. Torabi, G. Massé, and G.-A. Bilodeau, "An iterative integrated framework for thermal-visible image registration, sensor fusion, and people tracking for video surveillance applications," *CVIU*, 2012.
- [61] C. Li, H. Cheng, S. Hu, X. Liu, J. Tang, and L. Lin, "Learning collaborative sparse representation for grayscale-thermal tracking," *TIP*, 2016.
- [62] K. Takumi, K. Watanabe, Q. Ha, A. Tejero-De-Pablos, Y. Ushiku, and T. Harada, "Multispectral object detection for autonomous vehicles," in *ACM MM*, 2017.
- [63] Q. Ha, K. Watanabe, T. Karasawa, Y. Ushiku, and T. Harada, "Mfnet: Towards real-time semantic segmentation for autonomous vehicles with multi-spectral scenes," in *IROS*, 2017.
- [64] S. Hwang, J. Park, N. Kim, Y. Choi, and I. S. Kweon, "Multispectral pedestrian detection: Benchmark dataset and baselines," in *CVPR*, 2015.
- [65] K. Zhou, L. Chen, and X. Cao, "Improving multispectral pedestrian detection by addressing modality imbalance problems," in *ECCV*, 2020.
- [66] K. Takumi, K. Watanabe, Q. Ha, A. Tejero-De-Pablos, Y. Ushiku, and T. Harada, "Multispectral object detection for autonomous vehicles," in *TW ACM MM*, 2017.
- [67] H. Rezatofighi, N. Tsoi, J. Gwak, A. Sadeghian, I. Reid, and S. Savarese, "Generalized intersection over union: A metric and a loss for bounding box regression," in *CVPR*, 2019.
- [68] Z. Zheng, P. Wang, W. Liu, J. Li, R. Ye, and D. Ren, "Distance-iou loss: Faster and better learning for bounding box regression," in *AAAI*, 2020.
- [69] Z. Zhang, "Flexible camera calibration by viewing a plane from unknown orientations," in *ICCV*, 1999.
- [70] Z. Zhang, "A flexible new technique for camera calibration," *TPAMI*, 2000.
- [71] L. Wang, Y. Guo, Y. Wang, Z. Liang, Z. Lin, J. Yang, and W. An, "Parallax attention for unsupervised stereo correspondence learning," *TPAMI*, 2020.
- [72] D. Programmer, "Darklabel," <http://darkpgmr.tistory.com/16>, 2022.
- [73] K. Chen, J. Wang, J. Pang, Y. Cao, Y. Xiong, X. Li, S. Sun, W. Feng, Z. Liu, J. Xu, Z. Zhang, D. Cheng, C. Zhu, T. Cheng, Q. Zhao, B. Li, X. Lu, R. Zhu, Y. Wu, J. Dai, J. Wang, J. Shi, W. Ouyang, C. C. Loy, and D. Lin, "MMDetection: Open mmlab detection toolbox and benchmark," *ArXiv*, 2019.
- [74] K. He, X. Zhang, S. Ren, and J. Sun, "Deep residual learning for image recognition," in *CVPR*, 2016.
- [75] T.-Y. Lin, P. Dollár, R. Girshick, K. He, B. Hariharan, and S. Belongie, "Feature pyramid networks for object detection," in *CVPR*, 2017.
- [76] Y. Xinyi, L. Boyang, L. Ruoqing, W. Tianhao, and L. Ting, "Basicirstd," <https://github.com/XinyiYing/BasicIRSTD>, 2021.